Journal of Materials Chemistry A

ROYAL SOCIETY OF CHEMISTRY

PAPER

View Article Online
View Journal | View Issue

Check for updates

Cite this: J. Mater. Chem. A, 2024, 12, 26857

Environmentally responsible synthesis of high-performance P2-$Na_{2/3}[Ni_{1/3}Mn_{2/3}]O_2$ sodium-ion battery cathodes†

Jintao Fu, Mohamed H. Hassan, Jiaxin Liu, Hyeongjun Koh, Alexander K. Ng, Chiara Bruzzi, John S. Corsi and Eric Detsi *

P2-type $Na_{2/3}[Ni_{1/3}Mn_{2/3}]O_2$ (NNMO) is a promising Na-ion battery cathode for its high operation voltage, high gravimetric capacity, and low critical element content. Current methods to make NNMO, such as sol–gel, solid-state reaction, and spray pyrolysis, are not environmentally friendly, as they often use acetate and nitrate metal salt precursors, which release undesirable gaseous byproducts such as CO_2 and HNO_3 when these metal salts are heat-treated at high temperatures. Decarbonizing our industries and the transportation sector requires not only using batteries to store intermittent renewable energy, but also decarbonizing the synthesis methods to make key components of these batteries, *i.e.*, the electrode materials. Here, we demonstrate an environmentally responsible synthesis of NNMO by direct conversion of metallic Ni powder with various particle sizes (10 nm, 100 nm, 1 μm, 5 μm), a process that only releases O_2 and H_2O as byproducts, as opposed to the harmful gases released when nickel salts are used. The resulting NNMO made from ≈1 μm commercial Ni powder exhibits an excellent cycling performance as a Na-ion battery cathode. When cycled between 2-4 V *vs.* Na/Na^+, the material exhibits a rate-capability of ≈83 mA h g^{-1} at 10C (*i.e.*, > 96% theoretical capacity) and ≈ 78 mA h g^{-1} at 20C (*i.e.*, >90% theoretical capacity), together with a remarkable stability of 93% capacity retention after 500 cycles at 10C. When cycled between 1.3–4 V *vs.* Na/Na^+, the material shows a high initial capacity of ≈134 mA h g^{-1} at 2C, with a capacity retention of 57% after 500 cycles.

Received 28th May 2024
Accepted 3rd September 2024

DOI: 10.1039/d4ta03708a

rsc.li/materials-a

1. Introduction

Sodium-ion batteries (SIBs) have emerged as a promising alternative to Li-ion batteries (LIBs) due to the abundance of their constituent elements, such as Na and Mn, in contrast to LIBs, which heavily rely on critical elements such as Li and Co.[1] Among the different SIB components, cathode materials with fast Na storage kinetics, high operating potentials, and relatively high specific capacity are desirable.[2] To date, various types of cathode materials have been developed, including Prussian blue analogues,[3] polyanion compounds,[4] and layered transition metal oxides.[5] P2-type $Na_{2/3}[Ni_{1/3}Mn_{2/3}]O_2$ (NNMO), where "P" stands for Na occupying prismatic sites and "2" represents the number of transition metal layers in a repeating unit, is one of the most promising layered transition metal oxides offering a high operation voltage, a high specific capacity (173 mA h g^{-1} when all the 2/3 Na is (de)intercalated), and high air stability.[6] Furthermore, NNMO only contains 33 at% of Ni, its only critical element, as opposed to the state-of-the-art NMC 811 cathode which contains 80 at% Ni together with Li and Co.[7] Despite such advantages, the main challenge currently impeding the widespread adoption of NNMO as one of the next-generation cathode materials for SIBs is the structural change during cycling. Indeed, when cycled between 2–4.5 V *vs.* Na/Na^+, NNMO undergoes a P2–O2 phase transition, accompanied by >20% volume change, leading to capacity decay and cell failure.[8] Extensive research efforts have been directed towards mitigating issues related to this P2–O2 phase transition, which include strategies such as cation/anion doping,[9] protective layer coating,[10] and nanoengineering.[6]

On the other hand, less attention has been paid to issues related to the synthesis of NNMO. Traditional methods to make NNMO, such as sol–gel,[11] solid-state reaction,[10] and spray pyrolysis,[12] usually involve the use of metal salt precursors including nitrates and acetates, which subsequently release undesirable gaseous byproducts of NO_x (from nitrates) and CO_x (from acetates) when annealed at high temperature in air.[13,14] These emissions pose significant environmental hazards, contradicting the vision of clean and sustainable energy production. In this work, we introduce a novel protocol to fabricate P2-NNMO directly from metallic Ni and sodium permanganate ($NaMnO_4$). This protocol eliminates the need for nickel salts and the release of toxic gases, a common drawback in

Department of Materials Science & Engineering, University of Pennsylvania, Philadelphia, Pennsylvania 19104, USA. E-mail: detsi@seas.upenn.edu

† Electronic supplementary information (ESI) available. See DOI: https://doi.org/10.1039/d4ta03708a

conventional synthesis methods. In addition to the sustainable synthesis route, the resulting NNMO exhibits a remarkable cycling performance comparable to that of NNMO synthesized from a traditional approach. For example, when cycled between 2–4 V *vs.* Na/Na^+ (utilizing half of Na in the formula, and yielding ≈86 mA h g^{-1} theoretical capacity[15]), NNMO synthesized from commercial Ni powder with an average particle size of 1 μm delivers a specific capacity of ≈83 mA h g^{-1} at 10C (*i.e.*, >96% theoretical capacity) and ≈78 mA h g^{-1} at 20C (*i.e.*, > 90% theoretical capacity). Further, it exhibits outstanding cycling stability as well, retaining 93% of its original capacity after 500 cycles at 10C. When cycled in a broader voltage window of 1.3–4 V *vs.* Na/Na^+, the material shows a high initial capacity of ≈134 mA h g^{-1} at 2C, with a capacity retention of ≈80% after 180 cycles and ≈57% after 500 cycles. This combination of a sustainable synthesis approach and excellent electrochemical performance holds significant promise for advancing the development of next-generation SIB cathodes.

2. Experimental

2.1 Materials preparation

Four types of metallic Ni were utilized as precursors for the synthesis of P2-$Na_{2/3}[Ni_{1/3}Mn_{2/3}]O_2$. Three commercial Ni powders purchased from Sigma Aldrich and Thermo Scientific, comprised of (i) Ni nanopowder with 80–150 nm average particle size (99.8%, Thermo Scientific Chemicals), denoted as 100 nm Ni in this article; (ii) 1 μm Ni powder (99.8%, Sigma Aldrich); and (iii) Ni powder with 3–7 μm mean particle size (99.8%, Sigma Aldrich), denoted as 5 μm Ni in this article. The fourth type of Ni was nanoporous Ni (NP-Ni) fabricated by dealloying.[16] In doing so, we first prepared a $Ni_{30}Mn_{70}$ at% alloy ingot by mixing Ni powder (99.8%, Sigma Aldrich) and Mn powder (99.99%, Fisher Scientific) with a mass ratio of 1 : 2.2 and melting this mixture under an argon atmosphere using an electric arc-melter (EQ-SP-MSM207 from MTI). Afterward, the ingot was cold rolled into thin foils and immersed in 1 M ammonium sulfate solution for 6 days to fully dissolve the sacrificial Mn atoms by free corrosion dealloying. After dealloying, the product was thoroughly rinsed 5 times with Deionized (DI) H_2O, dried under vacuum overnight, and stored in air for NNMO synthesis.

In a typical NNMO synthesis process, 100 mg of metallic Ni powder was mixed with 560 mg of sodium permanganate monohydrate ($NaMnO_4 \cdot H_2O$) (97%, Sigma Aldrich) and 1 mL 1 M NaOH solution. The NaOH was used to provide an extra Na source to compensate for Na loss during high-temperature solid-state conversion.[10,12] The mixture was heated on a hot plate at 150 °C in air to evaporate water, followed by ball-milling in an agate jar (Across International) for one hour. An exception was made for the mixture containing 100 nm Ni as the sample was put into an agate jar without milling balls to avoid particle coarsening.[17] Finally, solid-state conversion was performed between 800 and 900 °C in a muffle furnace (Thermo Scientific) in air, followed by rapid cooling to room temperature.[18]

For comparison, NNMO was also synthesized using the traditional approach, by mixing metal salts of sodium, nickel, and manganese acetates. Specifically, sodium acetate trihydrate (2.1 mmol, Sigma Aldrich), nickel acetate tetrahydrate (1 mmol, Sigma Aldrich), and manganese acetate tetrahydrate (2 mmol, Sigma Aldrich) were dissolved in 3 mL DI H_2O. Oxalic acid (5.1 mmol, Sigma Aldrich) dissolved in 4 mL DI H_2O was added to the previous solution under stirring, forming a white precipitate. This mixture was heated to 90 °C until it became dry, and the collected powder was annealed at 500 °C for 5 h and then at 950 °C for 15 h in air with a heating rate of 2 °C min^{-1}.

In the following sections, the NNMO converted from NP-Ni, 100 nm Ni, 1 μm Ni, 5 μm Ni, and Ni acetate (NiAc) are denoted as NP-Ni-NNMO, 100 nm Ni-NNMO, 1 μm Ni-NNMO, 5 μm Ni-NNMO, and NiAc-NNMO, respectively.

2.2 Materials characterization

X-ray diffraction (XRD) was performed using a Rigaku Miniflex powder diffractometer (Cu X-ray source, operated at 40 kV/15 mA) with a 0.02° step size and a 4° min^{-1} scanning speed. The morphology of the starting metallic Ni and converted NNMO was studied by scanning electron microscopy (SEM) using a JEOL 7500F equipped with energy-dispersive X-ray spectroscopy (EDS). The chemical compositions of 1 μm Ni-NNMO and NiAc-NNMO were determined by inductively coupled plasma optical emission spectroscopy (Spectro Genesis ICP-OES device). Small-angle X-ray scattering (SAXS) was performed using a XENOCS Xeuss 2.0 Environmental X-ray Scattering instrument with dual copper and molybdenum X-ray sources at Penn, which has a detection limit between 1 Å and 570 nm.[19–23] Transmission electron microscopy (TEM) characterization was performed with JEOL F200 operated at 200 kV, with NNMO samples mixed with 3 mL of DI H_2O and drop-casted on lacey carbon TEM grids (Ted Pella). Zone axes such as [100] and [001] were carefully selected based on simulated Kikuchi patterns.[24,25] The selected area electron diffraction (SAED) patterns were captured at a dose rate of 5 $e^-/Å^2$ s for 1.2 s with a OneView camera (Gatan). High-resolution images were acquired at 400 $e^-/Å^2$ s for 0.6 s.

2.3 Electrochemical measurements

2032 type coin cells were assembled using NNMO slurry as working electrodes, Na metal as counter and reference electrodes, and glass microfiber (Whatman, Grade GF/C) as the separator in an argon-filled glove box (MBraun) with H_2O/O_2 content below 0.1 ppm. The NNMO slurry was prepared by homogeneously mixing 70 wt% active material (NNMO powder), 20 wt% carbon additives (equal mass of carbon black, carbon nanofibers, and graphene nanosheets), and 10 wt% binder (40 mg mL^{-1} of polyvinylidene fluoride dissolved in *N*-methyl-2-pyrrolidone), and was cast on Al foil current collector (18 μm thick, Fisher Scientific). The slurry coating was then dried under vacuum at room temperature overnight, followed by heating at 150 °C under argon atmosphere for 2 h to remove residual water. After drying, circular disks of the working electrode with active material loading 1.6 ± 0.4 mg cm^{-2} were cut with a disc cutter (MSK-T-09, MTI Corp). The electrolyte used in coin cells was 1 M sodium perchlorate in ethylene carbonate (EC)/

dimethyl carbonate (DMC) (1 : 1 by volume) with 5 vol% addition of fluoroethylene carbonate (FEC). All electrochemical tests were performed using a Biologic VMP-300 multichannel potentiostat. Electrochemical impedance spectroscopy (EIS) data were taken using AC voltage with an amplitude of 10 mV in a frequency range between 1 MHz and 10 mHz.

3. Results and discussion

3.1 Impact of the size of Ni metal precursor on the formation of NNMO

To make NNMO starting with metallic Ni, one needs to identify an appropriate source of Na, Mn, and O. Here, we use $NaMnO_4$ as the source of Na, Mn, and O, since $NaMnO_4$ can react with Ni at a Ni-to-$NaMnO_4$ molar ratio of 1 : 2 to form NNMO with the overall reaction as shown in eqn (1):

$$Ni\ (s) + 2NaMnO_4 \cdot H_2O\ (s) \rightarrow 3Na_{2/3}[Ni_{1/3}Mn_{2/3}]O_2\ (s) + 2H_2O\ (g) + O_2\ (g) \quad (1)$$

The initial stage of the reaction in eqn (1) involves the thermal decomposition of $NaMnO_4$ to form MnO_2 between 120–180 °C and Na_2MnO_3 between 540–580 °C, both of which are stable in air.[26] The major challenge of using metallic Ni as a precursor arises from the limited diffusion of Na and Mn species into the core of the Ni particles. To address this, we investigated the effect of metallic Ni precursors with various sizes, namely 10 nm Ni (NP-Ni), 100 nm Ni, 1 μm Ni, and 5 μm Ni, on the synthesis of NNMO. Fig. 1 shows the XRD profiles of converted NNMO. The relatively small sizes of NP-Ni and 1 μm Ni facilitated their complete conversion to NNMO after 24 h at 800 °C, as shown by the magenta and orange XRD curves, respectively. Notably, the present annealing condition (*i.e.*, 800 °C and 24 h) was identified as the minimal time and temperature to achieve the full conversion of NNMO, as lower temperature or shorter annealing time did not result in a full conversion (Fig. S1a†). While the 100 nm Ni nanopowder was converted to NNMO within only 1 h at 850 °C (Fig. S1b†) owing to its short diffusion length, persistent impurity peaks emerged even after extending the annealing time to 24 h at 800 °C (Fig. 1, green pattern). The impurity peaks match with $NaMnO_2$ (PDF#25-0845), as marked with triangle labels, and the origin of such impurities will be discussed in the next section. The 5 μm Ni was not completely converted to NNMO, even after 24 h at 800 °C, due to the increased diffusion length in bigger Ni particles. However, a higher temperature (900 °C) and a longer annealing time (72 h) led to enhanced (while not yet full) conversion, as shown by the dashed and solid blue curves, respectively. For comparison, the traditional synthesis route utilizing Ni acetate salt achieved complete conversion after 5 h at 500 °C followed by 15 h at 950 °C, as indicated by the purple pattern. Rietveld refinement is further performed on two samples, namely the 1 μm Ni-NNMO and NiAc-NNMO, Fig. S2.† The $d_{(002)}$ layer spacing is then extracted from the refined spectrum, which shows 5.57 Å for the 1 μm Ni-NNMO and 5.59 Å for the NiAc-NNMO (Fig. S2c†). These results are in agreement with the $d_{(002)}$ distance derived from Si powder calibrated XRD spectrum, which shows 5.59 Å for both the 1 μm Ni-NNMO and the NiAc-NNMO (Fig. S2d†). The values are smaller compared to the nominal (002) distance of 5.60 Å for NNMO, suggesting that our NNMO contains excess Na (enhanced electrostatic cohesions of O–Na–O leading to decreased layer spacing), as will be confirmed with the EDS/ICP composition analysis in a latter section.

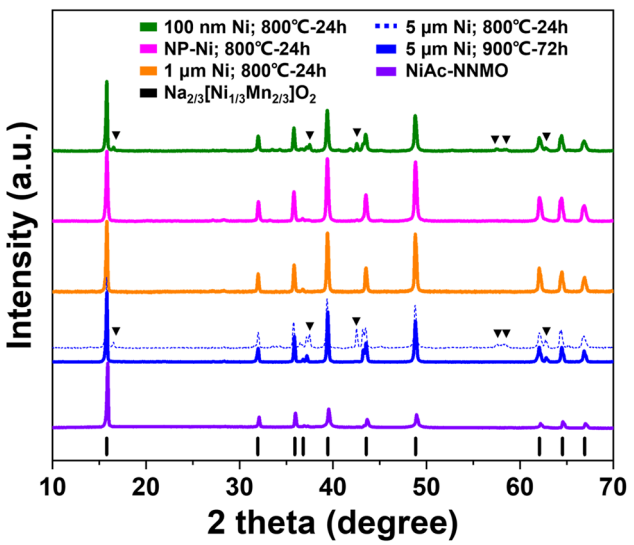

Fig. 1 XRD patterns of NNMO converted from different metallic Ni precursors. Under the annealing condition of 800 °C for 24 h, the 100 nm Ni (green) and 5 μm Ni (dashed blue) showed impurity peaks corresponding to $NaMnO_2$ (triangle labels), while the NP-Ni (magenta) and 1 μm Ni (orange) yielded full conversion. An enhanced (but not yet full) conversion was obtained for 5 μm Ni under the annealing condition of 900 °C for 72 h (solid blue). The NNMO prepared from Ni acetate salt using the traditional synthesis method yielded full conversion (purple).

The size of converted NNMO particles is critical for its cycling performance, as it directly impacts the Na diffusion length, which in turn impacts the rate capability. Therefore, SEM was used to investigate the morphology of the starting metallic Ni and the converted NNMO, as shown in Fig. 2. Although the initial size of the 100 nm Ni particles was in the nanoscale, the converted NNMO particles were much larger, with a characteristic "diameter" of approximately 1 μm (Fig. 2a). Further details on the variation of NNMO particle size obtained from 100 nm Ni under different heat-treatment conditions (1 h or 3 h at 850 °C) are provided in Fig. S3,† where it is seen that the ≈1 μm NNMO particles formed after 1 h of annealing remained relatively unchanged thereafter. Based on the reports on coarsening and densification of nanopowders during sintering,[27] we speculate that the 100 nm Ni particles coalesced into larger particles at the early stage of solid-state conversion, hindering the formation of nanoscale NNMO. In addition, this densification might impede Na and Mn diffusion, leading to incomplete conversion and the persistence of impurity phases even after extended annealing. The morphology of NP-Ni is characterized by nanoscale ligaments and pores with an approximate size of 10 nm (Fig. 2b). The presence of these nanoscale features was further confirmed with SAXS analysis, as

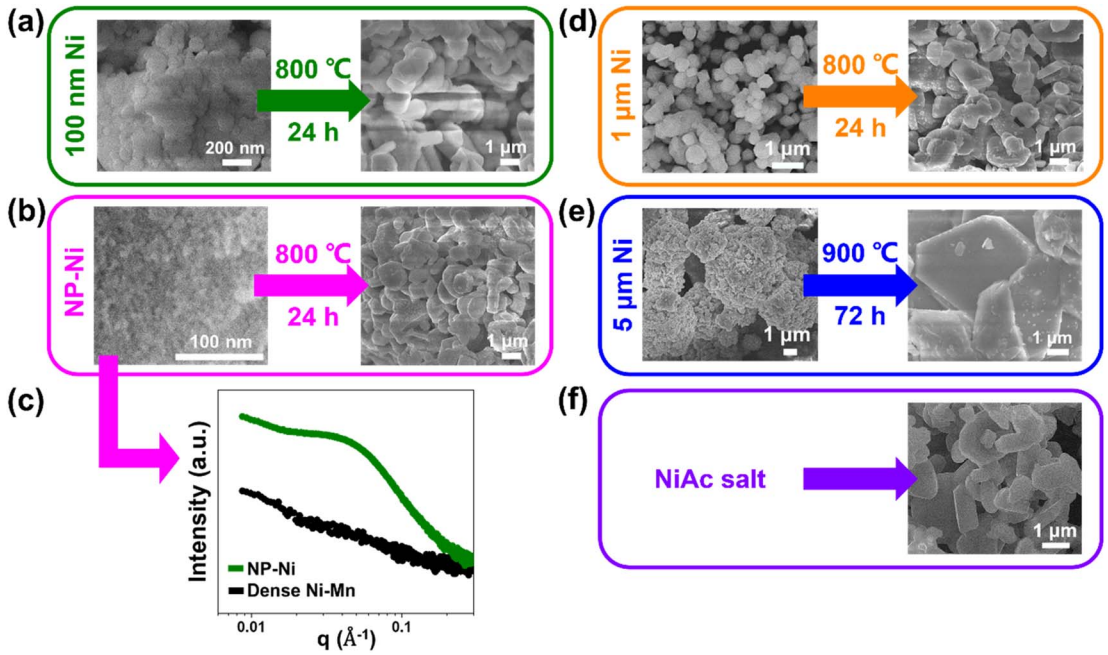

Fig. 2 SEM images comparing the morphology and size of starting Ni precursor and converted NNMO particles: (a) 100 nm Ni (left) and converted NNMO (right). (b) NP-Ni (left) and converted NNMO (right). (c) SAXS pattern confirming the presence of nanoscale features in NP-Ni. Compared to the absence of a scattering peak in the dense Ni-Mn parent alloy (black), NP-Ni (green) showed a characteristic peak centered around $q = 0.045$ Å^{-1}, which corresponds to a ligament/pore size of ≈9 nm. (d) 1 μm Ni (left) and converted NNMO (right). (e) 5 μm Ni (left) and converted NNMO (right). (f) Ni acetate salt converted NNMO. Despite various types of starting Ni, the minimal "diameter" of converted NNMO particles scales around 1 μm.

shown in Fig. 2c. The green curve representing the SAXS pattern of NP-Ni displays a characteristic peak centered around $q = 0.045$ Å^{-1}, which is absent in the dense Ni-Mn parent alloy before dealloying (black curve). This peak corresponds to a ligament–ligament distance (or pore–pore distance) of approximately 17 nm, as calculated using eqn (2):[23,28]

$$d\,(\text{ligament–ligament distance}) = 1.23 \times 2\pi/q \qquad (2)$$

Thus, the ligament/pore size is approximately 9 nm (corresponding to half of d in eqn (2)), which agrees with the SEM images. Following solid-state conversion, the previously observed nanoscale structures vanished, and were replaced by NNMO with plate-like morphology having a characteristic "diameter" of approximately 1 μm (Fig. 2b). The annealing temperature influenced the synthesized NNMO particle size, with higher temperatures (850 °C and 900 °C) leading to significantly larger NNMO particles (Fig. S4†). NNMO derived from 1 μm Ni (Figure 2d) and 5 μm Ni (Fig. 2e) precursors closely resembled the size of these starting materials. Regardless of the initial Ni precursor size (nano or micro), the minimum achievable characteristic "diameter" of the converted NNMO particles remained around 1 μm, which is among the smallest reported.[12,29,30] NNMO synthesized from Ni acetate salt also gave an average particle size of 1 μm (Fig. 2f). Dynamic light scattering (DLS) analysis is further performed on two samples, namely the 1 μm Ni converted NNMO and NiAc salt converted NNMO, Fig. S5.† The particle sizes derived from DLS analysis are in agreement with the SEM results. EDS and ICP were subsequently used to analyze the elemental composition of the synthesized NNMOs, Table 1. Compared to the stoichiometric ratio of Na : Ni : Mn = 40 : 20 : 40, the NP-Ni-NNMO and 1 μm Ni-NNMO have an average ratio of 42 : 18 : 40 and 48 : 15 : 37 from EDS, respectively. This indicates that while the NP-Ni-NNMO was close to the stoichiometric ratio, the 1 μm Ni-NNMO was rich in Na. The Na-rich composition in 1 μm Ni-NNMO is further confirmed with ICP, showing an average ratio of 62 : 13 : 25. A similar Na-rich composition is also observed for the NiAc-NNMO control sample, with an average ratio of 61 : 13 : 26. Such excess Na is responsible for their excellent electrochemical performances, as will be discussed in the next section.

Considering the limited conversion of 100 nm Ni-NNMO and the increased particle size of 5 μm Ni-NNMO, NNMOs derived from NP-Ni and 1 μm Ni appear particularly promising for usage as SIB cathodes. Thus, the nanostructures of NP-Ni-NNMO and 1 μm Ni-NNMO were further investigated using TEM. Both

Table 1 Elemental composition analysis of NNMOs based on EDS and ICP

Sample	Method	Na (at%)	Ni (at%)	Mn (at%)
Nominal	—	40	20	40
NP-Ni-NNMO	EDS	42	18	40
1 μm Ni-NNMO	EDS	48	15	37
	ICP	62	13	25
NiAc-NNMO	ICP	61	13	26

materials showed well-defined lattice fringes (Fig. 3a and d), indicative of a layered oxide structure. Additionally, EDS mapping revealed the homogeneous distribution of Na, Ni, and Mn elements across the structure, Fig. S6.† The SAED pattern acquired along the [001] axis (Fig. 3b and e) confirms the formation of a hexagonal structure, with the presence of satellite spots that are associated with Na^+-vacancy ordering.[31,32] The SAED pattern collected along the [100] axis (Fig. 3c and f) reveals the interlayer spacing available for Na intercalation. The (002) spacing is calculated to be 5.76 Å and 5.98 Å for NP-Ni-NNMO and 1 μm Ni-NNMO, respectively. This value is slightly larger than the nominal value of 5.60 Å,[12] likely due to variation in Na content within each cathode particle, resulting in small change in interlayer spacing. However, our XRD result in Fig. S2† suggests that the average interspacing is generally smaller among the cathode materials synthesized from different starting precursors.

3.2 Electrochemical performance of NNMO as SIB cathode material

3.2.1 Cycling between 2–4 V *vs.* Na/Na^+. Due to the incomplete conversion, the 100 nm Ni-NNMO was excluded from further electrochemical evaluation. The electrochemical performance of the remaining synthesized NNMO was evaluated in a half-cell configuration with a Na metal counter electrode. The cyclic voltammetry (CV) curves shown in Fig. 4a of NNMO obtained from NP-Ni, 1 μm Ni, 5 μm Ni, and Ni acetate salt showed two sets of characteristic redox peaks between 3–4 V *vs.* Na/Na^+, each of which is associated with the reversible (de)sodiation of 1/6 Na from NNMO in combination with Ni^{2+}/Ni^{3+} redox, yielding a theoretical capacity of ≈86 mA h g^{-1} between 2–4 V.[29] Further CV analysis in a broader voltage window (≈1.3–4.5 V *vs.* Na/Na^+) for NP-Ni-NNMO reveals additional redox peaks below 2 V *vs.* Na/Na^+ and above 4 V *vs.* Na/Na^+ (Fig. S7a†).[11] The former, below 2 V, corresponds to (de)sodiation of additional 1/3 Na in combination with Mn^{3+}/Mn^{4+} redox (which yields an additional theoretical capacity of ≈86 mA h g^{-1} between approximately ≈1.3–2 V), thus forming $Na[Ni_{1/3}Mn_{2/3}]O_2$ instead of $Na_{2/3}[Ni_{1/3}Mn_{2/3}]O_2$,[29] and the latter, above 4 V, corresponds to the reversible (de)sodiation of 1/3 Na from NNMO in combination with Ni^{3+}/Ni^{4+} redox, which yields a theoretical capacity of ≈86 mA h g^{-1} between 4–4.5 V. In other words, by cycling NNMO between ≈1.3–4.5 V *vs.* Na/Na^+, one could achieve a theoretical capacity of ≈259 mA h g^{-1}. Unfortunately, P2-O2 phase transitions occur in the voltage range 4–4.5 V, resulting in rapid capacity fading. Thus, the rapid decay in peak intensity from the CVs when NNMO is cycled up to 4.5 V suggests that our NNMO degrades due to P2-O2 phase transition. Therefore, the upper cycling window was set to 4 V *vs.* Na/Na^+ in the subsequent electrochemical measurements. In this section, we will first examine the cycling performance between 2–4 V *vs.* Na/Na^+ (with theoretical capacity ≈86 mA h g^{-1}) where only Ni redox reactions are active, and in the next section, we will extend the lower cut-off voltage to 1.3 V *vs.* Na/Na^+ (with theoretical capacity of ≈173 mA h g^{-1}) to include both the Ni and Mn redox reactions.

The rate-capability of 1 μm Ni-NNMO showed the best performance, followed by NNMO converted from Ni acetate salt, NP-Ni, and 5 μm Ni (Fig. 4b). The 5 μm Ni-NNMO showed a capacity decay at high rates (20C and 40C), which arise from the sluggish kinetics caused by the large particle size. The 1 μm Ni-NNMO achieved ≈83, 78, 65, and 90 mA h g^{-1} at 10C, 20C, 40C, and 2C, corresponding to ≈96, 90, 76, and 104% of the theoretical capacity, respectively. The excess capacity at 2C might be attributed to a minor capacitive contribution.[33] When

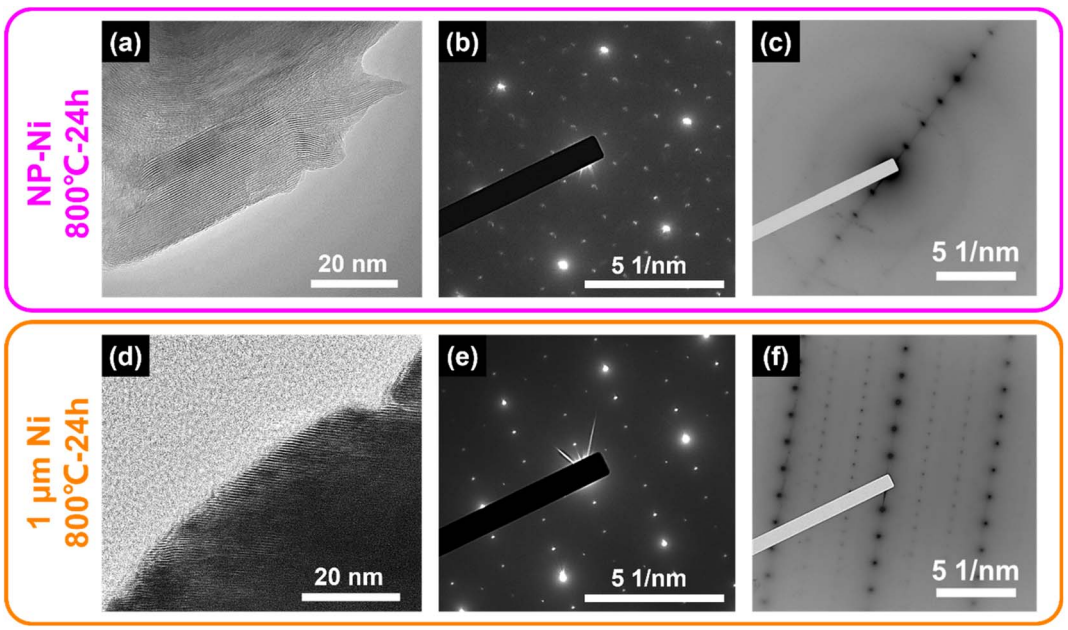

Fig. 3 TEM images of NNMO converted from NP-Ni (1st row) and 1 μm Ni (2nd row). Lattice fringes observed under high-resolution TEM (a and d), and corresponding SAED pattern along the [001] axis (b and e) showing hexagonal structure with Na^+-vacancy ordering. SAED patterns along the [100] axis reveal (002) layer spacings of 5.76 Å (c) and 5.98 Å (f), respectively.

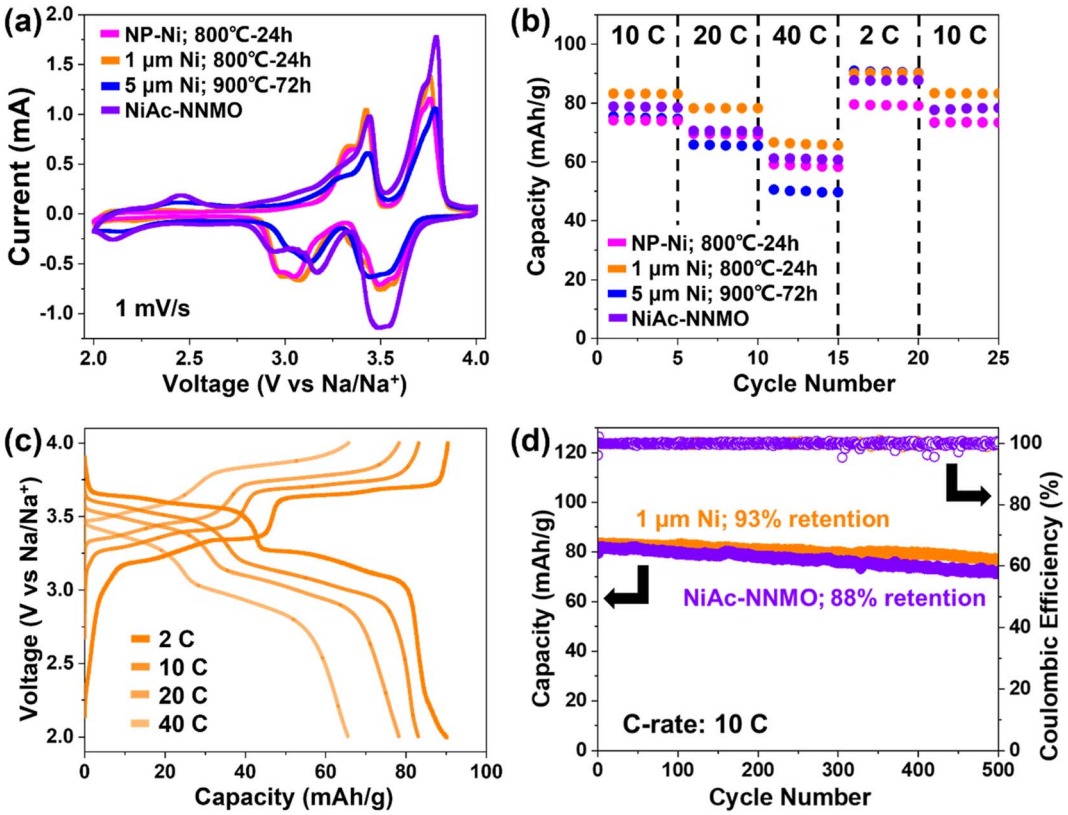

Fig. 4 (a) Cyclic voltammetry of NNMO converted from NP-Ni (magenta), 1 μm Ni (orange), 5 μm Ni (blue), and Ni acetate salt (purple) cycled between 2–4 V *vs.* Na/Na^+ under 1 mV s^{-1}. (b) Rate-capability of NNMO converted from NP-Ni (magenta), 1 μm Ni (orange), 5 μm Ni (blue), and Ni acetate salt (purple) cycled between 2-4 V *vs.* Na/Na^+, with the corresponding galvanostatic curves of 1 μm Ni-NNMO in (c). (d) Long-term cycling of NNMO at 10C between 2–4 V *vs.* Na/Na^+. NiAc-NNMO (purple) exhibited 88% capacity retention, and 1 μm Ni-NNMO (orange) achieved 93% capacity retention after 500 cycles.

the C-rate returned from 2C to 10C, the original capacity was fully recovered. The corresponding galvanostatic (dis)charge curves are shown in Fig. 4c for the 1 μm Ni-NNMO, with further data for NP-Ni-NNMO and NiAc-NNMO provided in Fig. S7b and S8,† respectively. The clear plateaus observed under all C-rates suggest that the charge storage process remains mostly faradaic, even during high-rate cycling.[34] Since the 1 μm Ni-NNMO and NiAc-NNMO showed the best (and comparable) performance, galvanostatic charge–discharge profiles of these NNMOs under slower C-rates (*i.e.*, 0.1C, 0.2C, 0.5C, and 1C) are also evaluated (Fig. S9†), and a normalized energy efficiency (taking the energy density of C/10 as 100% efficiency) is calculated based on the integration of the *E*–*Q* profile (Fig. S10†). The results show that both 1 μm Ni-NNMO and NiAc-NNMO can maintain >95% energy efficiency up to 1C, and >60% energy efficiency even at 40C, confirming their excellent rate-performance. Kinetic analysis performed on the NP-Ni-NNMO further reveals that the characteristic "b-value" is higher compared to literature reports, confirming the excellent rate performance (details on kinetics analysis shown in the ESI†). Fig. 5 represents a comparative analysis of the obtained rate-capability with previously reported data for P2-NNMO cycled within the same voltage window.[8,11,12,15,30,31,35–37] Our 1 μm Ni-NNMO achieved the highest capacity at C-rates exceeding 2C. This superior performance is attributed to the presence of excess Na in the NNMO structure,[38,39] as confirmed by EDS, ICP, XRD, and Rietveld refinement. Specifically, while a Na-rich composition in NNMO does not favor the layer spacing for

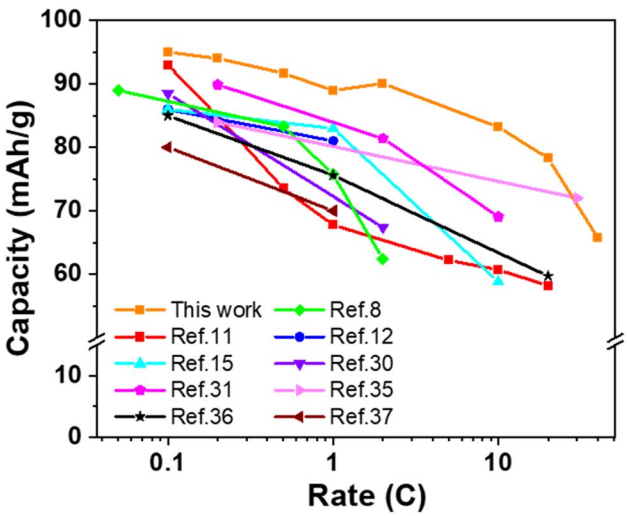

Fig. 5 Rate capability reported for P2-NNMO. All electrodes are cycled between 2–4 V *vs.* Na/Na^+.

Na^+ migration, it can contribute to the rate performance from two aspects: (i) Promote Ni^{2+} oxidation, such that more Ni^{2+} can participate in the charge compensation upon desodiation, thus providing more capacity within a given C-rate.[38] (ii) Increased Na_e/Na_f ratio, where Na_e and Na_f stand for Na^+ occupying the edge-sharing and face-sharing prismatic sites, respectively. Since Na_e sites have a higher Na^+ mobility, this increase in Na_e/Na_f ratio leads to improved rate performance.[39] Finally, the cycling stability was tested at 10C, evaluated for 1 μm Ni-NNMO and NiAc-NNMO, as shown in Fig. 4d, as well as in Fig. S5c† for NP-Ni-NNMO. Both exhibited similar initial capacity and stability, with 1 μm Ni-NNMO retaining ≈93% of its capacity after 500 cycles, corresponding to a minimal capacity decay of only ≈0.014% per cycle.

Electrochemical impedance spectroscopy (EIS) is further performed on the 1 μm Ni-NNMO and NiAc-NNMO, to evaluate the charge transfer resistance associated with the (de)sodiation at 2C. Fig. 6 shows the Nyquist plots consisting of depressed semicircles in the high and medium frequency regions, and a linear curve in the low frequency region. The former corresponds to the charge transfer resistance, while the latter corresponds to the Warburg diffusion.[40] The first cycle (pristine NNMO) shows a high charge transfer resistance, likely due to the poor electrolyte wetting in the as-assembled cell. After 30 cycles of charge–discharge at 2C, both NNMOs showed a similar resistance value of ≈350 Ω for discharge (*i.e.* sodiation, Fig. 6a and c) and ≈75 Ω for charge (*i.e.*, desodiation, Fig. 6b and d). The similar resistance seen in both NNMOs agrees with their comparable electrochemical performance. Notably, in both samples the impedance during discharge (Fig. 6a and c) was much larger than during charge (Fig. 6b and d). Similar observations have been reported previously in the case of $LiCoO_2$ tested as a LIB cathode.[41] This phenomenon can be attributed to the concentration gradient of Na^+ formed at the electrode–electrolyte interface, leading to an increased Na^+ intercalation resistance seen during discharge of NNMO.

3.2.2 Cycling between 1.3–4 V *vs.* Na/Na$^+$. Additional capacity can be obtained from NNMO when cycled below 2 V *vs.* Na/Na^+ arising from the Mn^{3+}/Mn^{4+} redox couple. Herein, we cycle the 1 μm Ni-NNMO (which showed the best performance in the range of 2–4 V *vs.* Na/Na^+) between 1.3–4 V *vs.* Na/Na^+ corresponding to a theoretical capacity of ≈173 mA h g^{-1}. Fig. 7a shows the first 10 CV curves cycled under 1 mV s^{-1}. While the redox peaks between 3–4 V *vs.* Na/Na^+ almost overlap, gradual peak intensity decay is observed for the redox peak below 2 V *vs.* Na/Na^+, as indicated by the black arrows. This decrease in peak intensity corresponds to a gradual capacity decay, as shown in Fig. 7b the galvanostatic curves of the first 20 cycles at 2C: from ≈134 mA h g^{-1} in the 1st cycle to ≈130 mA h g^{-1} in the 20th cycle. Previous studies on NNMO

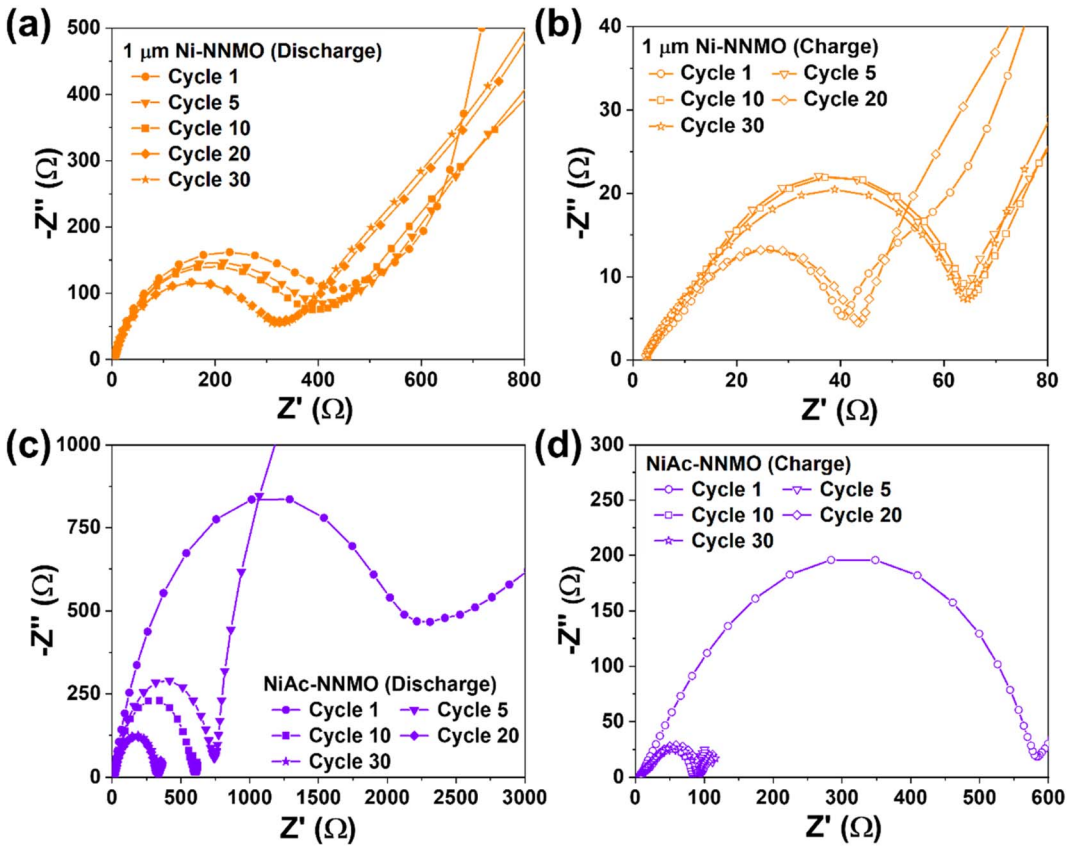

Fig. 6 Nyquist plots of NNMO electrodes after various (de)sodiation cycles. (a) 1 μm Ni-NNMO, discharge (sodiation), (b) 1 μm Ni-NNMO, charge (desodiation), (c) NiAc-NNMO, discharge (sodiation), (d) NiAc-NNMO, charge (desodiation). After stabilization, both samples showed similar charge transfer resistance of ≈350 Ω for discharge and ≈75 Ω for charge.

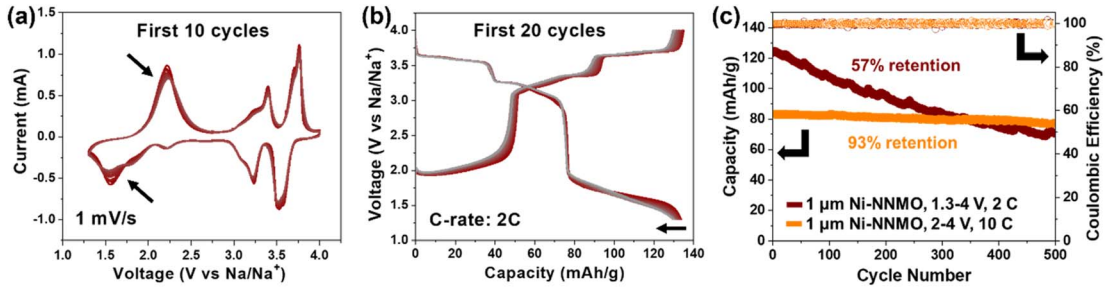

Fig. 7 (a) Cyclic voltammetry of 1 μm Ni-NNMO cycled between 1.3–4 V *vs.* Na/Na^+ under 1 mV s^{-1}. The peak intensity decay over 10 cycles (black arrows) indicates structural distortion caused by Jahn–Teller effect of Mn^{3+}. (b) Galvanostatic curves of 1 μm Ni-NNMO cycled between 1.3–4 V *vs.* Na/Na^+ under a C-rate of 2C. Gradual capacity decay is observed over 20 cycles. (c) Long-term cycling of 1 μm Ni-NNMO between 1.3–4 V *vs.* Na/Na^+ under a C-rate of 2C (brown), achieving 57% capacity retention after 500 cycles. In contrast, 1 μm Ni-NNMO cycled between 2–4 V *vs.* Na/Na^+ under a C-rate of 10C (orange) achieved 93% capacity retention after 500 cycles.

have also shown a performance degradation when the Mn^{3+}/Mn^{4+} redox couple is included,[42] which is known to originate from the Jahn–Teller effect, namely Mn^{3+} will distort the MnO_6 octahedron by elongating the longitudinal Mn–O bonds while shortening the horizontal Mn–O bonds.[43] Such structural distortion is detrimental to the cycling stability as shown in Fig. 7c: compared to the excellent stability of the 1 μm Ni-NNMO cycled between 2–4 V *vs.* Na/Na^+ (orange), the 1 μm Ni-NNMO cycled between 1.3-4 V *vs.* Na/Na^+ (brown) exhibited higher initial capacity but only retained ≈80% after 180 cycles and ≈57% after 500 cycles, despite a slower cycling rate (2C *vs.* 10C). Notably, elemental doping (*i.e.*, Mg, Zn) is known to suppress the Jahn–Teller effect and structural distortion,[43] which will be one of the future research directions.

4. Conclusion

This work presents an environmentally responsible synthesis route to P2-type $Na_{2/3}[Ni_{1/3}Mn_{2/3}]O_2$ by direct conversion of metallic Ni powder in the presence of sodium permanganate, a process that only releases O_2 and H_2O gases. Thus, the proposed method prevents the formation of undesirable byproducts such as HNO_3 and CO_2, commonly released when nickel salts (nitrates and acetates) are used as precursors. We have systematically studied the formation of P2-$Na_{2/3}[Ni_{1/3}Mn_{2/3}]O_2$ using metallic Ni powders with various average particle sizes, including 10 nm, 100 nm, 1 μm, and 5 μm, and found that P2-$Na_{2/3}[Ni_{1/3}Mn_{2/3}]O_2$ synthesized from Ni powder with an average particle size of 1 μm showed an excellent performance as a Na-ion battery cathode. When cycled between 2–4 V *vs.* Na/Na^+, the material exhibited a rate-capability of ≈83 mA h g^{-1} at 10C (*i.e.*, >96% theoretical capacity) and ≈78 mA h g^{-1} at 20C (*i.e.*, >90% theoretical capacity), together with a remarkable cycling stability of ≈93% capacity retention after 500 cycles at 10C. When cycled in a broader voltage window of 1.3–4 V *vs.* Na/Na^+, the material showed a high initial capacity of ≈134 mA h g^{-1} at 2C, with a capacity retention of ≈80% after 180 cycles and ≈57% after 500 cycles. These findings pave the way for the design and development of next-generation Na-ion battery cathodes.

Conflicts of interest

The authors declare no conflicts of interest.

Acknowledgements

The authors gratefully acknowledge the National Science Foundation (NSF) for their financial support through NSF-CAREER CMMI-2047851 and NSF FM-2134715. We gratefully acknowledge the National Science Foundation (NSFMRI-1725969), which funded the Dual Source (Cu and Mo) and Environmental X-ray Scattering (DEXS) facility used in this research. This work was carried out in part at the Singh Center for Nanotechnology, part of the National Nanotechnology Coordinated Infrastructure Program, which is supported by the NSF grant NNCI-2025608. Lastly, AI-assisted manuscript proofreading was performed using Grammarly.

References

1 C. Helbig, A. M. Bradshaw, L. Wietschel, A. Thorenz and A. Tuma, *J. Cleaner Prod.*, 2018, **172**, 274–286.
2 W.-J. Lv, Z. Huang, Y.-X. Yin, H.-R. Yao, H.-L. Zhu and Y.-G. Guo, *ChemNanoMat*, 2019, **5**, 1253–1262.
3 B. Xie, B. Sun, T. Gao, Y. Ma, G. Yin and P. Zuo, *Coord. Chem. Rev.*, 2022, **460**, 214478.
4 Q. Ni, Y. Bai, F. Wu and C. Wu, *Advanced Science*, 2017, **4**, 1600275.
5 P. Gupta, S. Pushpakanth, M. A. Haider and S. Basu, *ACS Omega*, 2022, **7**, 5605–5614.
6 Y. Liu, Q. Shen, X. Zhao, J. Zhang, X. Liu, T. Wang, N. Zhang, L. Jiao, J. Chen and L.-Z. Fan, *Adv. Funct. Mater.*, 2020, **30**, 1907837.
7 C. M. Julien and A. Mauger, *Energies*, 2020, **13**, 6363.
8 D. H. Lee, J. Xu and Y. S. Meng, *Phys. Chem. Chem. Phys.*, 2013, **15**, 3304–3312.
9 J. Zhang, W. Wang, W. Wang, S. Wang and B. Li, *ACS Appl. Mater. Interfaces*, 2019, **11**, 22051–22066.
10 Y. Liu, X. Fang, A. Zhang, C. Shen, Q. Liu, H. A. Enaya and C. Zhou, *Nano Energy*, 2016, **27**, 27–34.

11 Q. Liu, Z. Hu, M. Chen, C. Zou, H. Jin, S. Wang, Q. Gu and S. Chou, *J. Mater. Chem. A*, 2019, **7**, 9215–9221.
12 S. Y. Lee, J. H. Kim and Y. C. Kang, *Electrochim. Acta*, 2017, **225**, 86–92.
13 W. Brockner, C. Ehrhardt and M. Gjikaj, *Thermochim. Acta*, 2007, **456**, 64–68.
14 G. A. M. Hussein, A. K. H. Nohman and K. M. A. Attyia, *J. Therm. Anal.*, 1994, **42**, 1155–1165.
15 D. Yang, X.-Z. Liao, J. Shen, Y.-S. He and Z.-F. Ma, *J. Mater. Chem. A*, 2014, **2**, 6723–6726.
16 E. Detsi, J. B. Cook, B. K. Lesel, C. L. Turner, Y.-L. Liang, S. Robbennolt and S. H. Tolbert, *Energy Environ. Sci.*, 2016, **9**, 540–549.
17 B. Madavali, J.-H. Lee, J. K. Lee, K. Y. Cho, S. Challapalli and S.-J. Hong, *Powder Technol.*, 2014, **256**, 251–256.
18 O. Ruiz, M. Cochrane, M. Li, Y. Yan, K. Ma, J. Fu, Z. Wang, S. H. Tolbert, V. B. Shenoy and E. Detsi, *Adv. Energy Mater.*, 2018, **8**, 1801781.
19 S. S. Welborn and E. Detsi, *Nanoscale Horiz.*, 2020, **5**, 12–24.
20 J. Fu, J. S. Corsi, S. S. Welborn, V. Basile, L. Wang, A. K. Ng and E. Detsi, *ACS Sustain. Chem. Eng.*, 2021, **9**, 2762–2769.
21 T. Lee, H. Koh, A. K. Ng, J. Liu, E. A. Stach and E. Detsi, *Scr. Mater.*, 2022, **221**, 114959.
22 S. S. Welborn, J. S. Corsi, L. Wang, A. Lee, J. Fu and E. Detsi, *J. Mater. Chem. A*, 2021, **9**, 19994–20005.
23 A. K. Ng, S. S. Welborn and E. Detsi, *Scr. Mater.*, 2022, **206**, 114215.
24 A. D. Herron, S. P. Coleman, K. Q. Dang, D. E. Spearot and E. R. Homer, *MethodsX*, 2018, **5**, 1187–1203.
25 D. B. Williams and C. B. Carter, in *Transmission Electron Microscopy: A Textbook for Materials Science*, ed. D. B. Williams and C. B. Carter, Springer US, Boston, MA, 1996, pp. 3–17.
26 Z. Gontarz, R. Grzybowska and R. Sabaliński, *J. Therm. Anal.*, 1995, **45**, 1125–1133.
27 Z. Z. Fang, H. Wang and V. Kumar, *Int. J. Refract. Met. Hard Mater.*, 2017, **62**, 110–117.
28 J. Fu, S. Mooraj, A. K. Ng, C. Zhu, W. Chen and E. Detsi, *ACS Appl. Mater. Interfaces*, 2023, **15**, 27905–27914.
29 J. Mao, X. Liu, J. Liu, H. Jiang, T. Zhang, G. Shao, G. Ai, W. Mao, Y. Feng, W. Yang, G. Liu and K. Dai, *J. Electrochem. Soc.*, 2019, **166**, A3980.
30 G. Liu, L. Wen, Y. Li and Y. Kou, *Ionics*, 2015, **21**, 1011–1016.
31 Y. Shi, P. Jiang, S. Wang, W. Chen, B. Wei, X. Lu, G. Qian, W. H. Kan, H. Chen, W. Yin, Y. Sun and X. Lu, *Nat. Commun.*, 2022, **13**, 7888.
32 K. Kubota, T. Asari and S. Komaba, *Adv. Mater.*, 2023, **35**, 2300714.
33 H. Chu, Y. Pei, Z. Cui, C. Steven, P. Dong, P. M. Ajayan, M. Ye and J. Shen, *Nanoscale*, 2018, **10**, 14697–14704.
34 M. Li, T. Qiu, A. C. Foucher, J. Fu, Z. Wang, D. Zhang, A. M. Rappe, E. A. Stach and E. Detsi, *ACS Appl. Energy Mater.*, 2020, **3**, 11231–11241.
35 S. Wu, B. Su, K. Ni, F. Pan, C. Wang, K. Zhang, D. Y. W. Yu, Y. Zhu and W. Zhang, *Adv. Energy Mater.*, 2021, **11**, 2002737.
36 X. Zheng, P. Li, H. Zhu, K. Rui, G. Zhao, J. Shu, X. Xu, W. Sun and S. X. Dou, *Energy Storage Mater.*, 2018, **15**, 257–265.
37 M. R. D. Bomio, P. Lavela, A. A. G. Santiago, F. V Motta and J. L. Tirado, *Ceram. Int.*, 2023, **49**, 12452–12461.
38 C. Zhao, Z. Yao, Q. Wang, H. Li, J. Wang, M. Liu, S. Ganapathy, Y. Lu, J. Cabana, B. Li, X. Bai, A. Aspuru-Guzik, M. Wagemaker, L. Chen and Y.-S. Hu, *J. Am. Chem. Soc.*, 2020, **142**, 5742–5750.
39 S. Liu, J. Wan, M. Ou, W. Zhang, M. Chang, F. Cheng, Y. Xu, S. Sun, C. Luo, K. Yang, C. Fang and J. Han, *Adv. Energy Mater.*, 2023, **13**, 2203521.
40 M. Li, T. Qiu, S. S. Welborn, A. C. Foucher, J. Fu, B. K. Lesel, Z. Wang, L. Wang, E. A. Stach, A. M. Rappe and E. Detsi, *J. Mater. Chem. A*, 2024, **12**, 3671–3681.
41 H. Watanabe, S. Omoto, Y. Hoshi, I. Shitanda and M. Itagaki, *J. Power Sources*, 2021, **507**, 230258.
42 H. Wang, B. Yang, X.-Z. Liao, J. Xu, D. Yang, Y.-S. He and Z.-F. Ma, *Electrochim. Acta*, 2013, **113**, 200–204.
43 J. Feng, D. Fang, J. Li and J. Li, *Batteries Supercaps*, 2024, **7**, e202300476.